Full length article

Shock-induced amorphization in silicon carbide

S. Zhao [a, *], R. Flanagan [a], E.N. Hahn [a, b], B. Kad [a], B.A. Remington [c], C.E. Wehrenberg [c], R. Cauble [c], K. More [d], M.A. Meyers [a, **]

[a] University of California, San Diego, La Jolla, CA 92093, USA
[b] Los Alamos National Laboratory, Los Alamos, NM 87545, USA
[c] Lawrence Livermore National Laboratory, Livermore, CA 94550, USA
[d] Oak Ridge National Laboratory, Oak Ridge, TN 21005, USA

ARTICLE INFO

ABSTRACT

While silicon carbide (SiC) has been predicted to undergo pressure-induced amorphization, the microstructural evidence of such a drastic phase change is absent as its brittleness usually prevents its successful recovery from high-pressure experiments. Here we report on the observation of amorphous SiC recovered from laser-ablation-driven shock compression with a peak stress of approximately 50 GPa. Transmission electron microscopy reveals that the amorphous regions are extremely localized, forming bands as narrow as a few nanometers. In addition to these amorphous bands, planar stacking faults are observed. Large-scale non-equilibrium molecular dynamic simulations elucidate the process and suggest that the planar stacking faults serve as the precursors to amorphization. Our results suggest that the amorphous phase produced is a high-density form, which enhances its thermodynamical stability under the high pressures combined with the shear stresses generated by the uniaxial strain state in shock compression.

© 2018 Published by Elsevier Ltd on behalf of Acta Materialia Inc.

1. Introduction

The covalent bonding of silicon carbide (SiC) provides it with desirable properties such as high melting temperature, excellent corrosion resistance, as well as ultrahigh hardness. As such, it has been used as an important engineering material for load-bearing structures such as engine frames, body armor, fusion reactor components, and fiber/whisker-reinforced composites. SiC is also a semiconductor. Its high-temperature stability and high breakdown voltage render it a viable alternative for silicon-based electronic devices, especially in harsh service environments. Silicon carbide has a hexagonal 2H structure composed of Si-C pairs and is known to exhibit various polytypes which differ in the stacking sequence of the close-packed (basal) plane [1,2]. Whereas hcp metals have a simple ABAB sequence, the related 2H sequence is more complex: AaBbAaBb. Shih et al. [3] showed that dynamic compression generated changes in the stacking of these layers. It has also been reported that the 2H (referred to as α in previous literature)

structure can transform to other structures under quasi-static pressurization, and that the critical pressures for the phase transformations depend on the initial stacking sequence. For instance, it was shown that cubic 3C-Si (referred to as β in the literature, with a stacking sequence of AaBbCc) transforms to a NaCl-type structure (rock-salt) at around 100 GPa [3]. Chen et al. [4] performed in-situ nanopillar compression of hexagonal 4H-SiC and demonstrated a phase transformation to the 3C-SiC structure at 9-10 GPa. Furthermore, earlier studies suggest that SiC may undergo pressure-induced amorphization [5]. Amorphization of α SiC has been observed after 2 MeV electron [6] and 1.5 MeV Xe [7] irradiation. This was also observed in β SiC [8]. Recently, such a phase change was reported by Levitas et al. [9] in a diamond anvil cell experiment where torsion was superimposed with pressure. Levitas [10] developed a theory considering the effects of both hydrostatic and shear stresses on phase transformations. In static high-pressure experiments combining pressure and shear (through torsion) they determined, by X-ray diffraction, the formation of a high-density amorphous phase for α SiC. They emphasize that this is in large part due to the importance of shear, which decreases the threshold for amorphization and other transformations by a factor of 3–5. Han et al. [11] also reported deformation-induced amorphization in SiC nanowire, indicating that such a crystalline-

to-amorphous transition gives rise to the observed superplasticity.

Molecular dynamics calculations using the Tersoff potential by Mizushima et al. [12] as well as Tang and Yip [13] demonstrated that amorphization can take place at high pressures in cubic SiC. They evaluated both the phase transformation to the rock-salt structure and amorphization in terms of the shear moduli. A criterion of zero shear modulus was applied, which predicted two possible outcomes: when the tetragonal shear modulus goes to zero, transformation to rock salt structure occurs; when the rhombohedral shear modulus goes to zero, the result is amorphization.

Nanomachining of α SiC by Patten et al. [14] generated both brittle and ductile chips; the latter were analyzed by TEM and are proposed to be amorphous. This crystalline-to-amorphous transformation was proposed to be responsible for the brittle-to-ductile transition in SiC.

In addition to the quasi-static mechanical behavior, the response of SiC to dynamic loading and shock compression/release has also drawn great interest. Grady [15] studied the shock-wave response of polycrystalline silicon carbide and found that it exhibits a high Hugoniot elastic limit (HEL~15-16 GPa), after which it exhibits post-yield hardening, in contrast with B_4C where post-yield softening is usually observed. Shih et al. [16,17] studied the high rate deformation and shear localization of bulk and powder silicon carbide and found that the fracture mechanism depends on the particle size distribution. Feng et al. [18] measured the shear strength of shocked SiC and confirmed that it increases up to double the HEL, beyond which SiC gradually loses its strength with increasing shock compression. Li et al. [19] studied the spall behavior of mono and nanocrystalline SiC and concluded that the latter has a much lower spall strength. Such anomalous macroscopic behavior may be due to the conflicting microscopic phase changes that are often unreported in the literature [20,21]. However, the microstructural evidence of these shock-induced phase transitions has not been identified.

The systematic evaluation of the mechanochemistry of phase transformations and of amorphization, in particular by Levitas [10], provides a rationale for the importance of shear and its profound effect on the thermodynamics. This analysis is confirmed by the results of pressure-shear experiments which show the formation of a high-density amorphous phase. The fact that shock compression generates, by nature of the uniaxial strain state imposed, simultaneous and coupled hydrostatic and shear stresses has an important bearing on phase transformations. The goal of the current investigation is to establish whether shock compression, and its associated pressure and shear stresses, can generate amorphization in SiC.

2. Methods

2.1. Laser shock recovery experiments

To probe for evidence of phase transition, we performed laser shock recovery experiments at Janus Laser Facility, Lawrence Livermore National Laboratory. The Janus laser can generate large amplitude stress pulses with nanosecond duration, sufficient to shock silicon carbide above its phase transition threshold and to prevent it from shattering under shock compression and release. The 2Ω laser (~50 J) has a nominal square pulse shape with a (half width maximum wavelength) duration of 3 ns, resulting in a peak power of 1.67 TW/cm^2. Such a high energy density was deposited onto a target package which is comprised of an aluminum foil (200 μm) placed in front of a [0001] oriented 4-H monocrystalline SiC (3 mm in diameter and 1 mm in height, Fig. 1A). The ionization of the Al foil produces a high pressure that drives the shock wave into the SiC target. A copper capsule and momentum trap were

used to capture the reflected tensile stress waves. The acoustic impedance (product of density and sound velocity) of copper ($= 4.3 \times 10^7$ kg/m^{2}s) is close to that of SiC ($= 4.2 \times 10^7$ kg/m^{2}s). This further decreases unwanted tensile reflections and helps to ensure the integrity of the specimens. The shock parameters were determined by a separate VISAR experiment (Fig. 1B–D) and subsequent impedance matching (Fig. 1E) [22]. The rear (free) surface velocity (U_{fs}) of the free-standing aluminum foil subjected to a similar laser shock was characterized by velocity interferometry (VISAR). U_{fs} can be approximated as twice of the particle velocity (U_p), U_{fs} ~2 U_p. Conservation of momentum gives the relationship between the initial density ρ_o, particle velocity U_p, shock velocity U_s, and longitudinal stress or shock pressure, σ_{33}, as $\sigma_{33} = \rho_0 U_s U_p$. The shock pressure on the surface of silicon carbide is determined by shock impedance Z ($Z = \rho_0 U_s$ [22]) matching: at the interface of Al and silicon carbide, the shock wave is reflected and the shock pressure changes as equilibrium is reached. The inverted shock Hugoniot of Al gives the estimate of the reflected curve. Intersection of the reflected Al curve with shock Hugoniot of silicon carbide yields the estimate of the shock stress σ_s in the front surface of silicon carbide. Taking $U_p = 2.1$ km/s from Fig. 1D, one obtains $\sigma_s = 45$-50 GPa.

2.2. Microstructural characterization

After being subjected to laser shock compression, the recovered targets were examined by high resolution transmission electron microscopy (TEM), using a Hitachi HF3300 machine operated at 300 kV. TEM samples were cut directly from the shocked surface by a Hitachi focused ion beam (FIB) with a 30 kV initial high voltage for initial thinning and 2 kV low voltage for the final polishing. The TEM sample was then subjected to 900 V low energy ion milling (Fishione 1040 NanoMill) to remove the FIB damage.

2.3. Molecular dynamics simulations

Molecular dynamics simulations of silicon carbide were performed using LAMMPS [23] employing a modified Stillinger-Weber potential parameterized by Vashishta et al. [24]. Shock conditions were produced using a controlled piston driving along the [0001] axis for direct comparison to the experimental work. Transverse directions have periodic boundary conditions, creating a uniaxial strain shock [25]. Visualizations of simulation results were created using OVITO [26] employing the 'identify diamond structure' [27] and polyhedral template matching [28] tools. The selected Vashishta potential includes a three-body term intended to model the structural changes of SiC under pressure while maintaining bond-bending and bond-stretching characteristics. In past experiments and simulations, 3C SiC (cubic with the periodicity of 3 Si-C double layers) has been shown to undergo a phase transformation to 2H (hexagonal with the periodicity of 2 Si-C double layers) and rock-salt structure when subjected to pressures ranging from 70 to 140 GPa [24,29].

3. Results and discussion

3.1. Characterization

High-resolution transmission electron microscopy (TEM) revealed the post-shock microstructure. Localized amorphous bands (marked as a-SiC), with thickness up to 5 nm, can be identified. These bands can be either perpendicular (Fig. 2A) or inclined (Fig. 2B) to the direction of shock-wave propagation, which is in consistent with the c axis of the crystal. For the inclined amorphous band, there seem to be some lattice shifts in the vicinity of the band as shown by the inverse Fourier transformation diagram in Fig. 2C,
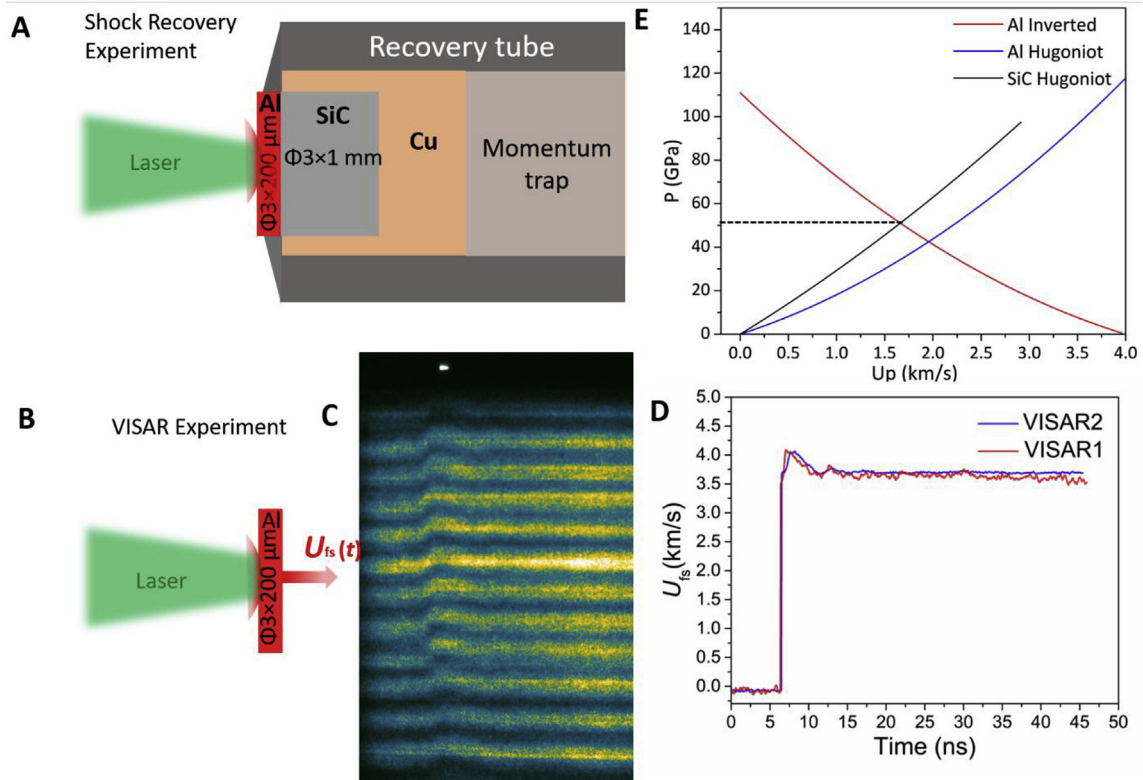
Fig. 1. Laser shock-recovery assembly, free surface velocity interferometry (VISAR), and determination of shock parameters. (A) Schematic drawings of the shock recovery experiment and (B) VISAR experiment. (C) Temporally resolved VISAR fringes, showing the shock break-out and pull-back features. (D) Free surface velocity, U_{fs} vs. T profiles. Two independent VISAR channels with distinctive Etalon length were used to unambiguously determine the free surface velocity. Peak U_{fs} ~4.2 km/s, rendering U_p~1/2 U_{fs} = 2.1 km/s. (E) Determination of shock stress by impedance match shock Hugoniot (σ_s vs. U_p) of aluminum and silicon carbide.
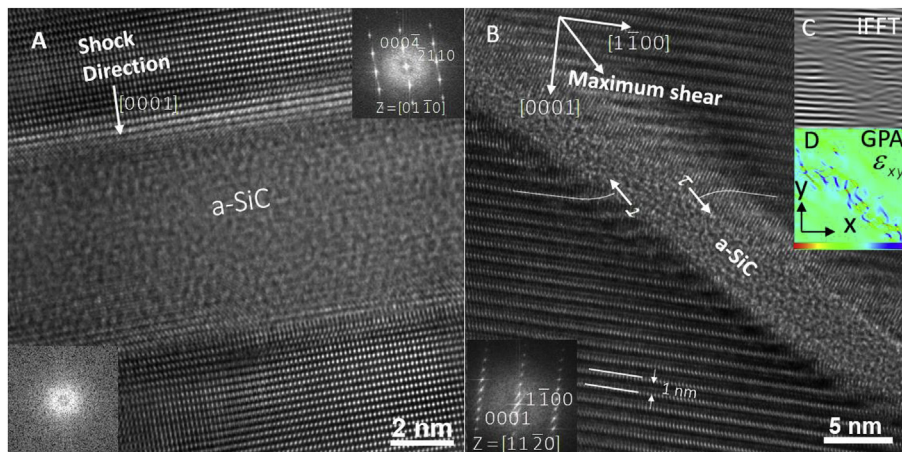

Fig. 2. TEM/HRTEM micrographs of recovered silicon carbide from laser shock compression. (A) An amorphous band perpendicular to the directional of shock wave propagation. (B) An inclined amorphous band shows lattice distortion/rotation at the crystalline/amorphous interface. (C) The Fourier filtered image of (B), using (0001) reflection. (D) Corresponding geometric phase analysis shows the deviatoric strain field in the vicinity of the amorphous band.

suggesting that this region has undergone drastic shear deformation. Graphic phase analysis (GPA) in Fig. 2D confirms that the in-plane shear strain is localized within the amorphous band. The inclined amorphous band shows a very similar morphology to the ones previously reported in Si [30,31], Ge [32], and B$_4$C [33]. However, the horizontal amorphous band is unexpected, as there is no resolved shear stress on the basal plane. One plausible explanation is that the horizontal bands are formed when inclined bands intersect with the plane of the TEM sample, as schematically shown

in Fig. S1 in the Supplementary data section. This hypothesis is supported by our MD simulations. Note that these amorphous bands are usually contiguous to nanocracks, suggesting that amorphization may be associated with the failure of SiC subjected to shock compression.

In addition to the two types of amorphous bands, planar faults have also been identified, which are likely to be the precursors to the amorphization. Fig. 3A illustrates the planar faults (indicated by the red triangles and magnified in the inset on the upper right
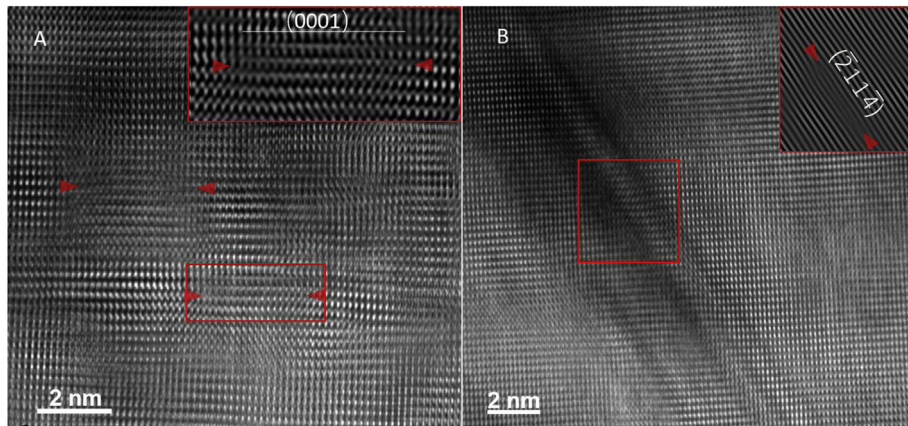
Fig. 3. Planar faults produced by shock deformation. (A) horizontal faults lying on (0001) planes; (B) inclined faults lying roughly on $(\overline{2}11\overline{4})$ planes.

corner) on the (0001) plane, i.e. the basal plane of SiC. Fig. 3B depicts another set of planar faults lying on the $(\overline{2}11\overline{4})$ planes. The lattice distortion caused by the planar faults is shown clearly in the Fourier filtered diagram in the upper right inset of Fig. 3B.

3.2. Molecular dynamics predictions

Large-scale MD simulations were performed to understand the three-dimensional structural evolution as a function of time. Fig. 4A shows a MD snapshot of the 81 GPa shock corresponding to a particle velocity, U_p, of 2.4 km/s. The higher shock pressure used in the simulations is required to activate plasticity at the higher strain rate. A perspective view of the simulation is given in Fig. 4A, which

shows the three-dimensional nature of the defects. Atomic structures are identified using nearest and second nearest neighbor distances, and then matching those structures to known lattice types such as diamond cubic [5]. The method is able to accurately identify the interlaced diamond cubic and hexagonal diamond structures that comprise the stacking series of 4H-SiC. Additionally, the algorithm is able to differentiate stacking faults and the boundaries between unidentified regions and the parent 4H lattice. The region within the bands could not be identified and is marked as "other" by the calculation. A portion of these atoms are amorphous in nature; a second set of atoms belong to small nano-crystallites of several phases, which will be thoroughly evaluated in subsequent work.
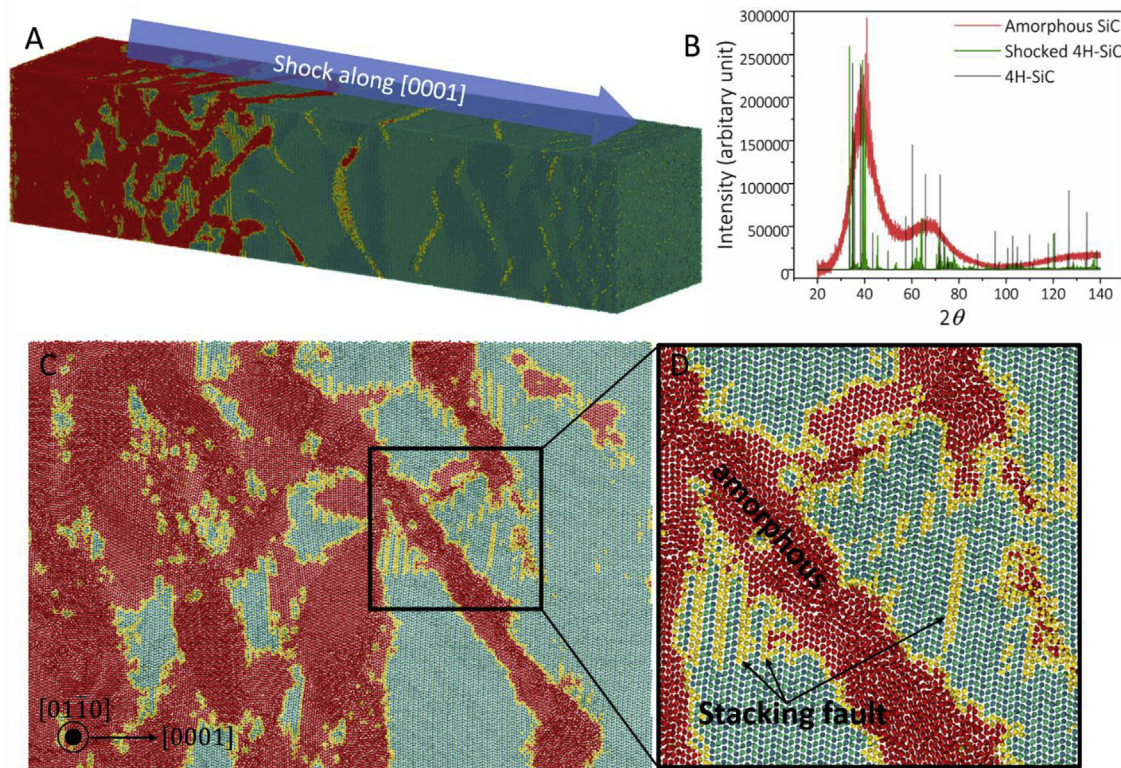
Fig. 4. Molecular dynamics simulations of 4H silicon carbide under shock compression. A depicts the complete phase change under 90 GPa. B shows the simulated X-ray diffraction of both perfect crystalline and amorphous material. C and D resemble slices of TEM images showing the embedding of the amorphous bands bounded by stacking faults in the perfect crystal.

In order to confirm the presence of an amorphous phase quantitatively, a virtual diffraction technique (developed by Coleman et al. [34]) was used as a post-processing step. The simulated diffraction uses 0.1541838 nm as the wavelength of incident radiation; the reciprocal space was subdivided into ~20 million nodes for the calculation. Structure factors for Si and C atoms are given by Peng et al. [35]. Fig. 4B shows the simulated powder diffraction patterns of 4H-SiC (black), the shocked 4H-SiC (green), and amorphous SiC phase (red) due to the extensive broadening of the peaks.

Fig. 4s. C and D are directly comparable to our TEM analysis in Fig. 2 and correspond to thin slices of the [01$\bar{1}$0] normal direction. The two slices illustrate a profuse amount of basal stacking fault activity as well as considerable lattice rotation. The interface between the amorphous bands and the remaining parent 4H crystal consists of stacking faults as large as the basal lattice constant, c_o. Longer shear bands tend to form parallel to the basal plane, as shown in Fig. 4D, as well as diagonally, corresponding to the maximum resolved shear stress direction. Deviatoric stresses relax locally as amorphous bands form, indicating that the phase change is driven by the large shear stresses. This shear stress leads to the formation of many stacking faults, which eventually interact, pile up, and form nuclei for amorphization. Since the amorphous region is the result of stacking-fault accumulation, and the main difference between polymorphs is their stacking sequence along the basal plane, it is reasonable to postulate that these intermediate phases are metastable and are precursors to amorphization.

The formation of an amorphous band is sequenced in Fig. 5. As the shock front passes through the material at 6.5 ps, small stacking faults are created as a result of the shear stresses. By 8.5 ps, new stacking faults have been generated as the old ones grow larger and thicker. Eventually, as shown at 10.5 ps, the stacking faults coalesce to form amorphous regions, which then expand into amorphous bands spanning the basal plane, as shown at 12.5 ps.

The local density of the material can be calculated by summing up the number of Si and C atoms in a known/specified volume and multiplying by their respective masses. Fig. 6 displays a snapshot of the system colored by normalized density, where $\rho/\rho_0 = 1$ corresponds to the uncompressed 4H density. The density of the amorphous regions is 6.4% greater than the density of the surrounding, compressed, 4H structure. This indicates that the amorphous phase is a high-density variant, the importance of which will be discussed in the following section.

3.3. Analysis

It is postulated that the shock-induced amorphization in SiC is a synergy of longitudinal shock and deviatoric stresses. The passage of a strong shock wave plastically deforms the crystalline lattice and introduces anisotropic defects such as planar faults, which may harden the material following the HEL. Upon a subsequent increment in loading, the material undergoes amorphization. It has been reported that the amorphous SiC is much more compliant than its crystalline counterpart [7]. Thus, a decrease in strength is expected if horizontal amorphization occurs in SiC. Additionally, the inclined amorphous banding is a result of shear localization which corresponds to the softening of the material. During the release stage, both horizontal and inclined amorphous bands are more prone to failure, as they create interfaces inside the crystal, which are preferred sites for cracks to nucleate and grow upon arrival of the reflected tensile pulses. This explains why the amorphous domains are usually found close to the cracks. It is interesting to note that Patten et al. [14] reported amorphization during nanomachining of monocrystalline SiC and actually observed that the corresponding chips were much longer than the untransformed ones. This suggests that amorphization plasticizes the material and renders it more ductile. This result is consistent with earlier findings by Grady [36] who reports post-yield hardening of the SiC subjected to dynamic loading.

The amorphization under shock compression was previously analyzed for Si, Ge, and B$_4$C [24–26]. The same formalism can be applied here, based on the effects of pressure and shear stresses on the thermodynamics of phase equilibria. The Patel-Cohen rationalization was applied to Si and it has the following form [37]:
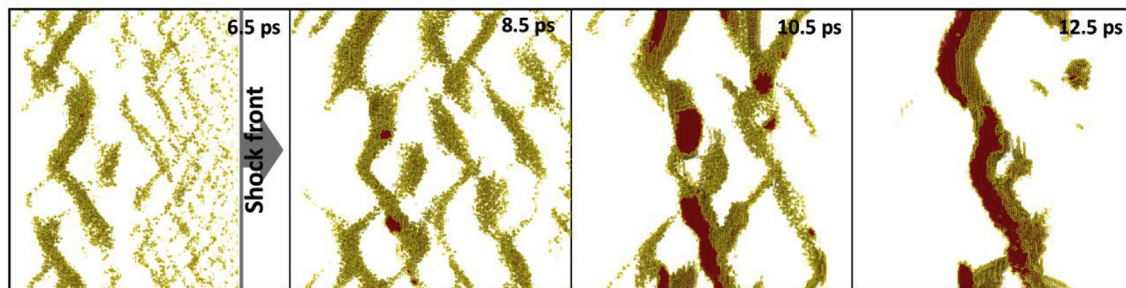

Fig. 5. The formation of an amorphous band in MD simulation. At 6.5 ps, the shock front has just passed through this portion of the material. 2 ps later, larger stacking faults form as smaller stacking faults pile up. At 10.5 ps, amorphous spots begin to form, eventually leading to the formation of an amorphous band as shown at 12.5 ps.
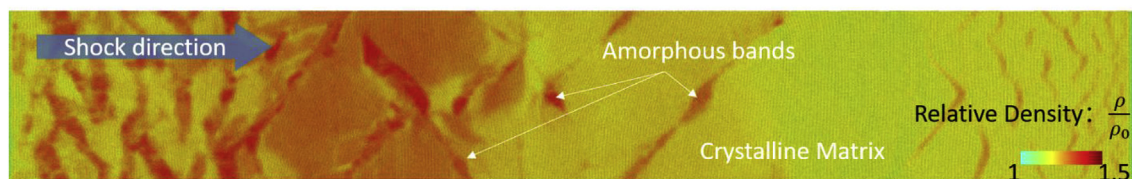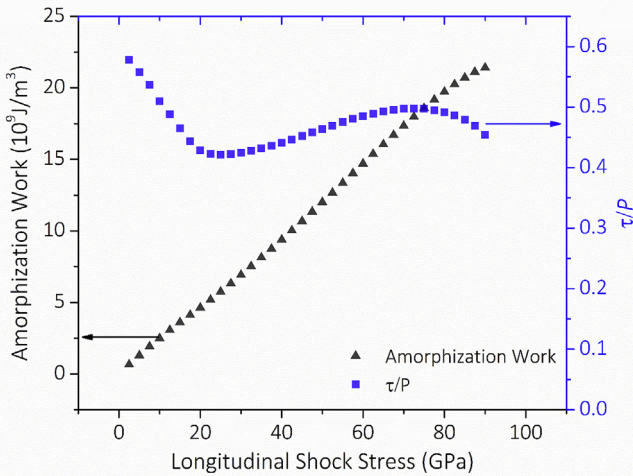

Fig. 6. MD simulation shows that the transformed region has a higher density with respect to their surroundings, indicating that the amorphous SiC is denser than the crystalline SiC at the corresponding shock condition. The figure is colored by the relative density, ρ/ρ_0.

Fig. 7. Effect of longitudinal shock stress on the amorphization work and ratio between the shear and hydrostatic components of shock stress.

$$W = P\varepsilon_T + \tau\gamma. \tag{1}$$

where P is the pressure (hydrostatic component of stress), ε_T is the amorphization normal strain, τ is the shear stress (here we assume maximum shear 45° away from the loading direction), and γ is the amorphization shear strain. The shear (maximum) and hydrostatic components of the stress are connected, for a hexagonal structure in which the shock propagation direction is [0001] through:

$$\frac{\tau}{P} = \frac{3(C_{33} - C_{13})}{2(2C_{13} + C_{33})}. \tag{2}$$

$C_{13} = 52$ GPa, $C_{33} = 553$ GPa are the elastic stiffness constants for the 4H structure (at ambient pressure) [38], rendering $\tau/P \approx 1.13$. Note that these elastic constants are, on their turn, dependent on pressure. The ratio τ/P as a function of longitudinal shock stress is shown in Fig. 7 from Hugoniostat calculations of 4H SiC over a time period of purely elastic loading [39]. Note that the interatomic potential underestimates the τ/P ratio as compared with the experimental results.

The Patel-Cohen methodology is a simplified approach to study the non-equilibrium transformation. Recently, a more rigorous phase transformation work criterion based on lattice instability has been proposed by Levitas et al. [40] and is consistent with our analysis. They applied a Landau-type theory rather than the one by Born and developed a general expression for the work of transformation for different states of stress. The predictions of this theory were compared with molecular dynamics simulations and applied to the Si(I)→Si(II) transformation. The expression for the critical 'modified' transformation work criterion is, for a simplified stress system where there are only normal stresses acting on the cube (which is the one in shock compression):

$$W = a_1\sigma_0\varepsilon_{0t} + a_2\boldsymbol{S} : \varepsilon_t \geq A(T) \tag{3}$$

where ε_{0t} is the spherical and ε_t the deviatoric component of strain in a stress-free transformation, σ_0 is the mean stress $((\sigma_{11}+\sigma_{22}+\sigma_{33})/3)$ and $\boldsymbol{S}$ is the deviatoric stress tensor, a_1 and a_2 are material parameters which dictate the evolution of one structure to the other. $A(T)$ is a critical temperature (T) dependent value that has to be overcome for the transformation to take place. If one assumes that both parameters evolve equally, $a_1 = a_2$. The similarity between Eqns. (2) and (3) becomes obvious. The generalized theory

by Levitas et al. [40] has the advantage of incorporating the complexities of transformation and shock compression.

Levitas et al. [9] obtained experimental results using static pressure shear loading which confirmed amorphization; they proposed the existence of a high-density amorphous phase (HDA) with a density higher than the crystalline counterpart. These results are corroborated by the present MD simulations, as shown in Fig. 6. The amorphous phase (red) has a density that is 6.4% higher than the crystalline one (yellow). Note that the relative density is also a function of shock stress; here we only consider the density at the onset of amorphization. This is the normal amorphization strain ε_T. The determination of the shear strain is less accurate. Whereas for silicon it was taken as the twinning strain, for B$_4$C it was assumed to be equal to the global shear strain divided by the fraction of the material that was amorphized. This latter assumption corresponds to the total relaxation of the shear inside the amorphized bands. In the current experiments we could not establish the separation between the shear transformation bands and therefore an arbitrary strain has to be assumed; it is taken to be equal to the twinning strain for the hexagonal structure, approximately 0.7. Inserting these values into Eqn. (1), one obtains the relationship described graphically in Fig. 7. The increase in W with shock stress is monotonic and reaches a value of 12.5 GJ/m^3 at 50 GPa, the experimental pressure. This provides the driving energy that overcomes the activation barrier and nucleates the amorphous bands. Note that our MD simulation suggests that under shock release, the structure of the high-density amorphous phase may relax to a lower density phase. However, this dynamic process cannot be captured by shock-recovery experiments, and further in-situ investigation should be carried out to elucidate this poly'a'morphism.

4. Conclusions

Shock compression was applied to monocrystalline α SiC along the [0001] direction through the use of short duration pulsed lasers which generate a pressure of ~50 GPa. The uniaxial strain state imparted by the shock is responsible for an associated shear stress of ~25 GPa. The combination of coupled hydrostatic and shear stresses under these loading conditions is responsible for the nucleation and movement of stacking faults, revealed both by transmission electron microscopy and MD simulations. Additionally, narrow bands (5–10 nm) of amorphized SiC are also observed and their presence is attributed to the periodic relaxation of deviatoric stresses.

Grady [15] observed strain-hardening in shock deformation of SiC; this is in contrast with boron carbide which was shown to exhibit strain-softening. We should point it out that Grady's classical experiments were conducted using a gas gun, which produces at least one order of magnitude longer time scale compared with our ns-laser driven shock experiments. The deformation mechanisms can be quite different in these two types of experiments. We actually believe that the fraction transformed will significantly increase for longer times. Strain hardening is usually related to defect-induced plasticity. In our study, we have shown that partial dislocations can be generated prior to amorphization, which will contribute to the strain hardening. However, amorphous banding usually is not considered a strain hardening mechanism. On the contrary, we proposed (and this is supported by other researchers) that amorphization causes the strain softening of boron carbide. The fact that cracks are contiguous to these amorphous bands also suggests that amorphization is related to loss of strain hardening ability. It is possible that the amorphization is much less extensive in SiC than in B$_4$C and therefore the softening is replaced by strain hardening due to stacking faults.

Observations are compared with MD calculations which also show the presence of these bands, albeit with smaller thickness and spacing. Their interior consists of a mixture of amorphous and nanocrystalline regions and they form preferentially near planes where the shear stress is maximum (45^0 to shock propagation direction). Although shear stress plays the dominant role in triggering amorphization, the contribution of hydrostatic pressure should not be ignored: (1) the work performed by pressure lowers the energy barrier between the two phases when the amorphous phase has a higher density than the crystalline one and (2) the confinement pressure prevents the sample from shattering.

The formation of these bands is preceded by generation and emission of stacking faults, as shown in the MD sequence of Fig. 6. As these stacking faults interact and as additional ones are generated on parallel planes a critical energy level is reached at which the material amorphizes and/or breaks up into nanocrystalline domains.

Our observations and calculations are consistent with the discovery of a high-density form of amorphous phase in SiC by Levitas et al. [9]. The amorphous phase revealed by MD calculations has a density ~6.4% higher than the 4H-SiC phase and thus suggests a negative Clapeyron slope for its formation, i.e., a decrease in the amorphization temperature with pressure. The application of the Patel-Cohen rationalization thus predicts that the high-pressure amorphous phase is favored at high pressures and shear stresses.

Acknowledgement

Appendix A. Supplementary data

Supplementary data related to this article can be found at https://doi.org/10.1016/j.actamat.2018.07.047.

References

[1] T.L.D. Aulton, T.J.B. Ernatowicz, R.S.L. Ewis, S.M. Essenger, F.J.S. Tadermann, S.A. Mari, Polytype Distribution of Circumstellar Silicon Carbide: Microstructural Characterization by Transmission Electron Microscopy, vol.67, 2003, pp. 4743—4767, https://doi.org/10.1016/S0016-7037(03)00272-2.

[2] G.R. Fisher, P. Barnes, Towards a Unified View of Polytypism in Silicon Carbide, 2016, p. 2812, https://doi.org/10.1080/13642819008205522.

[3] M. Yoshida, A. Onodera, M. Ueno, K. Takemura, O. Shimomura, Pressure-induced phase transition in SiC, Phys. Rev. B 48 (1993) 10587—10590, https://doi.org/10.1103/PhysRevB.48.10587.

[4] B. Chen, J. Wang, Y. Zhu, X. Liao, C. Lu, Y.W. Mai, S.P. Ringer, F. Ke, Y. Shen, Deformation-induced phase transformation in 4H-SiC nanopillars, Acta Mater. 80 (2014) 392—399, https://doi.org/10.1016/j.actamat.2014.07.055.

[5] A. Size, B. Covalent, PH YS ICAL REVIEW Atomic Size Effects in Pressure-induced of a Binary Covalent Lattice, vol.75, 1995, pp. 2738—2741.

[6] H. Inui, H. Mori, H. Fujita, Electron-irradiation-induced crystalline to amorphous transition in α-Sic single crystals, Philos. Mag. A B 61 (1990) 107—124, https://doi.org/10.1080/13642819008208655.

[7] W.J. Weber, L.M. Wang, N. Yu, N.J. Hess, Structure and properties of ion-beam-modified (6H) silicon carbide, Mater. Sci. Eng. 253 (1998) 62—70, https://doi.org/10.1016/S0921-5093(98)00710-2.

[8] H. Inui, H. Mori, A. Suzuki, H. Fujita, Electron-irradiation-induced crystalline-to-amorphous transition in β-SiC single crystals, Philos. Mag. A B 65 (1992) 1—14, https://doi.org/10.1080/13642819208223042.

[9] V.I. Levitas, Y. Ma, E. Selvi, J. Wu, J.A. Patten, High-density Amorphous Phase of Silicon Carbide Obtained under Large Plastic Shear and High Pressure, vol.54114, 2012, pp. 1—5, https://doi.org/10.1103/PhysRevB.85.054114.

[10] V.I. Levitas, High - pressure mechanochemistry: conceptual multiscale theory and interpretation of experiments, Phys. Rev. B 70 (2004) 184118, https://doi.org/10.1103/PhysRevB.70.184118.

[11] X.D. Han, Y.F. Zhang, K. Zheng, X.N. Zhang, Z. Zhang, Y.J. Hao, X.Y. Guo, J. Yuan, Z.L. Wang, Low-temperature in situ large strain plasticity of ceramic SiC nanowires and its atomic-scale mechanism, Nano Lett. 7 (2007) 452—457, https://doi.org/10.1021/nl0627689.

[12] K. Mizushima, S. Yip, E. Kaxiras, Ideal crystal stability and pressure-induced phase transition in silicon, Phys. Rev. B 50 (1994) 14952—14959, https://doi.org/10.1103/PhysRevB.50.14952.

[13] M. Tang, S. Yip, Atomic size effects in pressure-induced amorphization of a binary covalent lattice, Phys. Rev. Lett. 75 (1995) 2738—2741.

[14] J. Patten, W. Gao, K. Yasuto, Ductile regime nanomachining of single-crystal silicon carbide, J. Manuf. Sci. Eng. 127 (2005) 522, https://doi.org/10.1115/1.1949614.

[15] D.E. Grady, Shock-wave strength properties of boron carbide and silicon carbide, J. Phys. IV 4 (1994) 385—391, https://doi.org/10.1051/jp4:1994859.

[16] C.J. Shih, M.A. Meyers, V.F. Nesterenko, High-strain-rate deformation of granular silicon carbide, Acta Mater. 46 (1998) 4037—4065.

[17] C.J. Shih, V.F. Nesterenko, M.A. Meyers, High-strain-rate deformation and comminution of silicon carbide Characterization and evaluation of silicon carbide for high-velocity impact High-strain-rate deformation and comminution of silicon carbide, J. Appl. Phys. 83 (1998) 4660—4671, https://doi.org/10.1063/1.1468903.

[18] R. Feng, G.F. Raiser, Y.M. Gupta, Material strength and inelastic deformation of silicon carbide under shock wave compression, J. Appl. Phys. 83 (1998) 79, https://doi.org/10.1063/1.366704.

[19] W.H. Li, X.H. Yao, P.S. Branicio, X.Q. Zhang, N.B. Zhang, Shock-induced spall in single and nanocrystalline SiC, Acta Mater. 140 (2017) 274—289, https://doi.org/10.1016/J.ACTAMAT.2017.08.036.

[20] T. Sekine, T. Kobayashi, Shock compression of 6H polytype SiC to 160 GPa, Phys. Rev. B 55 (1997) 8034—8037.

[21] H. He, T. Sekine, T. Kobayashi, Direct transformation of cubic diamond to hexagonal diamond, Appl. Phys. Lett. 81 (2002) 610—612, https://doi.org/10.1063/1.1495078.

[22] M.A. Meyers, Dynamic Behavior of Materials, John Wiley & Sons, 1994.

[23] S. Plimpton, Fast parallel algorithms for short-range molecular dynamics, J. Comput. Phys. 117 (1995) 1—19, https://doi.org/10.1006/jcph.1995.1039.

[24] P. Vashishta, R.K. Kalia, A. Nakano, J.P. Rino, Interaction potential for silicon carbide: a molecular dynamics study of elastic constants and vibrational density of states for crystalline and amorphous silicon carbide, J. Appl. Phys. 101 (2007) 103515, https://doi.org/10.1063/1.2724570.

[25] B.L. Holian, P.S. Lomdahl, Plasticity induced by shock waves in nonequilibrium molecular dynamics simulations, Science 280 (80) (1998) 2085—2088, https://doi.org/10.1126/science.275.5302.955.

[26] A. Stukowski, Visualization and analysis of atomistic simulation data with OVITO—the Open Visualization Tool, Model. Simulat. Mater. Sci. Eng. 18 (2010) 15012, https://doi.org/10.1088/0965-0393/18/1/015012.

[27] E. Maras, O. Trushin, A. Stukowski, T. Ala-Nissila, H. Jonsson, Global transition path search for dislocation formation in Ge on Si (001), Comput. Phys. Commun. 205 (2016) 13—21.

[28] P.M. Larsen, S. Schmidt, J. Schiøtz, Robust structural identification via polyhedral template matching, Model. Simulat. Mater. Sci. Eng. 24 (2016) 55007, https://doi.org/10.1088/0965-0393/24/5/055007.

[29] W.H. Lee, X.H. Yao, W.R. Jian, Q. Han, High-velocity shock compression of SiC via molecular dynamics simulation, Comput. Mater. Sci. 98 (2015) 297—303, https://doi.org/10.1016/J.COMMATSCI.2014.11.029.

[30] S. Zhao, B. Kad, E.N. Hahn, B.A. Remington, C.E. Wehrenburg, C.M. Huntington, M. Bringa, K.L. More, M.A. Meyers, Pressure and shear induced amorphization of silicon, Extrem. Mech. Lett. 5 (2015) 74—80.

[31] S. Zhao, E.N. Hahn, B. Kad, B. a. Remington, C.E. Wehrenberg, E.M. Bringa, M. a. Meyers, Amorphization and nanocrystallization of silicon under shock compression, Acta Mater. 103 (2016) 519—533, https://doi.org/10.1016/j.actamat.2015.09.022.

[32] S. Zhao, B. Kad, C.E. Wehrenberg, B.A. Remington, E.N. Hahn, K.L. More, M.A. Meyers, Generating gradient germanium nanostructures by shock-induced amorphization and crystallization, Proc. Natl. Acad. Sci. Unit. States Am. 114 (2017) 201708853, https://doi.org/10.1073/pnas.1708853114.

[33] S. Zhao, B. Kad, B.A. Remington, J.C. LaSalvia, C.E. Wehrenberg, K.D. Behler, M.A. Meyers, Directional amorphization of boron carbide subjected to laser shock compression, Proc. Natl. Acad. Sci. Unit. States Am. (2016) 201604613, https://doi.org/10.1073/pnas.1604613113.

[34] S.P. Coleman, M.M. Sichani, D.E. Spearot, A computational algorithm to produce virtual x-ray and electron diffraction patterns from atomistic simulations, JOM (J. Occup. Med.) 66 (2014) 408—416, https://doi.org/10.1007/s11837-013-0829-3.

[35] L.M. Peng, G. Ren, S.L. Dudarev, M.J. Whelan, IUCr, robust parameterization of elastic and absorptive electron atomic scattering factors, Acta Crystallogr. Sect. A Found. Crystallogr. 52 (1996) 257—276, https://doi.org/10.1107/S0108767395014371.

[36] D.E. Grady, Hydrodynamic Compressibility of Silicon Carbide through Shock Compression of Metal - Ceramic Mixtures Hydrodynamic Compressibility Compression of Metal-ceramic of Silicon Carbide Mixtures through Shock, 1996, p. 197, https://doi.org/10.1063/1.355883.

[37] J.R. Patel, M. Cohen, Criterion for the action of applied stress in the martensitic transformation, Acta Metall. 1 (1953) 531–538.

[38] K. Kamitani, M. Grimsditch, J.C. Nipko, C.-K. Loong, M. Okada, I. Kimura, M. Grimsditch, The elastic constants of silicon carbide: a Brillouin-scattering study of 4H and 6H SiC single crystals, J. Appl. Phys. 82 (1997), https://doi.org/10.1121/1.1918627, 103515–2324.

[39] R. Ravelo, B.L. Holian, T.C. Germann, P.S. Lomdahl, Constant-stress Hugonio-stat method for following the dynamical evolution of shocked matter, Phys. Rev. B 70 (2004) 14103.

[40] V.I. Levitas, H. Chen, L. Xiong, Lattice instability during phase transformations under multiaxial stress:Modified transformation work criterion, Phys. Rev. B 96 (2017) 54118.